

Is atomic carbon a good tracer of molecular gas in metal-poor galaxies?

Simon C. O. Glover^{1,*} & Paul C. Clark²

¹ *Universität Heidelberg, Zentrum für Astronomie, Institut für Theoretische Astrophysik, Albert-Ueberle-Strasse 2, 69120 Heidelberg, Germany*

² *School of Physics and Astronomy, Queen's Buildings, The Parade, Cardiff University, Cardiff, CF24 3AA*

15 September 2018

ABSTRACT

Carbon monoxide (CO) is widely used as a tracer of molecular hydrogen (H₂) in metal-rich galaxies, but is known to become ineffective in low metallicity dwarf galaxies. Atomic carbon has been suggested as a superior tracer of H₂ in these metal-poor systems, but its suitability remains unproven. To help us to assess how well atomic carbon traces H₂ at low metallicity, we have performed a series of numerical simulations of turbulent molecular clouds that cover a wide range of different metallicities. Our simulations demonstrate that in star-forming clouds, the conversion factor between [C I] emission and H₂ mass, X_{CI} , scales approximately as $X_{\text{CI}} \propto Z^{-1}$. We recover a similar scaling for the CO-to-H₂ conversion factor, X_{CO} , but find that at this point in the evolution of the clouds, X_{CO} is consistently smaller than X_{CI} , by a factor of a few or more. We have also examined how X_{CI} and X_{CO} evolve with time. We find that X_{CI} does not vary strongly with time, demonstrating that atomic carbon remains a good tracer of H₂ in metal-poor systems even at times significantly before the onset of star formation. On the other hand, X_{CO} varies very strongly with time in metal-poor clouds, showing that CO does not trace H₂ well in starless clouds at low metallicity.

Key words: galaxies: ISM – ISM: clouds – ISM: molecules – stars: formation

1 INTRODUCTION

Giant molecular clouds (GMCs) play a central role in the life of our own and other galaxies, as they are the sites where essentially all star formation occurs. For this reason, the study of the formation and evolution of GMCs is a highly important topic. However, this study is hampered by the fact that the two main constituents of the gas making up a GMC – molecular hydrogen (H₂) and atomic helium – do not emit radiation at the low gas temperatures present in most GMCs. In order to study the molecular gas, it is therefore necessary to observe emission from less abundant chemical species that do emit at low temperatures and that are correlated with the H₂ distribution.

One of the most popular such tracer species is carbon monoxide (CO). This has several advantages as a tracer of molecular gas. First, there is a lot of it in most GMCs: it is typically the second most abundant molecular species, after H₂. Second, it emits readily at low temperatures: the energy separation between the rotational ground state ($J = 0$) and the first rotationally excited level ($J = 1$) is only

5.5 K. In addition, the main chemical pathways that lead to the formation of CO in the interstellar medium all involve H₂ as a key ingredient at some point (see e.g. the detailed discussion of CO formation chemistry in Glover et al. 2010), and so we would not expect large amounts of CO to form in regions devoid of H₂.

Observationally, CO emission has indeed proved to be a good tracer of molecular gas within the Milky Way. A number of different studies, summarized in the recent review by Bolatto, Wolfire & Leroy (2013), have shown that on scales comparable to or larger than individual GMCs there is a good correlation between the velocity-integrated intensity in the $J = 1 \rightarrow 0$ line of ¹²CO and the H₂ column density. The conversion factor from integrated intensity to column density – the so-called X-factor – is given approximately by

$$X_{\text{CO,MW}} = 2 \times 10^{20} \text{ cm}^{-2} (\text{K km/s})^{-1} \quad (1)$$

for Milky Way GMCs, and similar values are also found for other nearby, Milky Way-like disk galaxies. Simulations of GMCs in environments similar to that of the local ISM typically yield values for X_{CO} close to this observationally determined value (see e.g. Glover & Mac Low 2011; Shetty et al. 2011a,b; Narayanan et al. 2011; Narayanan & Hopkins

* E-mail: glover@uni-heidelberg.de

2013). Its lack of significant variation from cloud to cloud can be understood as a consequence of the fact that the main cloud properties that determine X_{CO} in metal-rich galaxies – the velocity dispersion, the temperature and the surface density of the gas – do not vary much from cloud to cloud (Narayanan & Hopkins 2013).

However, in low metallicity systems such as dwarf galaxies, CO is much less useful as a tracer of molecular gas. A growing number of observational studies have provided evidence that X_{CO} increases substantially as the metallicity decreases (see e.g. Israel 1997; Madden et al. 1997; Leroy et al. 2007, 2011; Gratier et al. 2010; Bolatto et al. 2011; Smith et al. 2012), owing to the reduction in the mean extinction of the molecular gas (see e.g. Glover & Mac Low 2011). Numerical simulations also suggest that the X_{CO} may become strongly time-dependent at low metallicity (Glover & Clark 2012b; see also Section 3.2 below). Furthermore, CO has proved to be extremely difficult to detect in very low metallicity systems: at $Z \leq 0.1 Z_{\odot}$, there are secure detections of CO in only two systems, the Wolf-Lundmark-Melotte and Sextans A dwarf galaxies (Elmegreen et al. 2013; Shi et al. 2015).

In view of the difficulties involved with using CO as a tracer of molecular gas in metal-poor galaxies, it is natural to ask whether there are better tracers that we might use. One interesting possibility is neutral atomic carbon, C. This produces two fine structure lines in its electronic ground state, the $^3P_1 \rightarrow ^3P_0$ transition at $609\mu\text{m}$ and the $^3P_2 \rightarrow ^3P_1$ transition at $370\mu\text{m}$. Its potential as a tracer of molecular gas was championed by Papadopoulos, Thi & Viti (2004), who pointed out that although simple PDR models predict that it will be confined to a thin transition region at the edge of molecular clouds (see e.g. Langer 1976), observations do not bear this out, and have long shown that C and CO emission are surprisingly well correlated in local clouds (Frerking et al. 1989; Little et al. 1994; Schilke et al. 1995; Kramer et al. 2008). This behaviour can be understood as a consequence of clumpy substructure within molecular clouds: CO emission comes primarily from within clumps and filaments, while [C I] emission traces their surfaces, but since the typical scale of the structures is small and there are often many along each line of sight, the result is that the projected CO and [C I] emission are well-correlated, both spatially and also in terms of velocity (Stutzki et al. 1988; Genzel et al. 1988; Plume, Jaffe & Keene 1994; Kramer et al. 2004; Glover et al. 2015).

More recently, Offner et al. (2014) have explored the usefulness of atomic carbon as a molecular gas tracer in solar metallicity clouds. They used the 3D-PDR code (Bisbas et al. 2012) to post-process simulations of turbulent molecular clouds, allowing them to predict the chemical composition and temperature of the gas at each point in the cloud. Based on this, they then computed synthetic emission maps for the $609\mu\text{m}$ of [C I] and the $J = 1 \rightarrow 0$ transition of CO, using the RADMC-3D radiation transfer code.¹ They found that [C I] emission was indeed a good tracer of H_2 column density in their model clouds. They also computed a mean [C I]-to- H_2 conversion factor, X_{CI} , for their models, and showed

that $X_{\text{CI}} = 1.1 \times 10^{21} \text{cm}^{-2} (\text{K km/s})^{-1}$ for a cloud with solar metallicity illuminated by the standard interstellar radiation field (ISRF), and $X_{\text{CI}} = 1.2 \times 10^{21} \text{cm}^{-2} (\text{K km/s})^{-1}$ for a solar metallicity cloud illuminated by a ten times stronger ISRF. However, Offner et al. (2014) did not explore whether X_{CI} is sensitive to the metallicity of the gas. In addition, there are a couple of inconsistencies in the Offner et al. (2014) approach that may influence their results. Firstly, they perform their hydrodynamical simulations assuming an isothermal equation of state (Offner et al. 2013), and only solve for the actual temperature distribution during the later post-processing step. This is a reasonable approximation in dense, well-shielded gas, but not in the lower density, moderately shielded gas where atomic carbon dominates (c.f. their Figures 6 and 7). Secondly, they evolve the chemistry for a period of 10 Myr, but stop the hydrodynamical simulation after ~ 1 Myr. They may therefore miss important non-equilibrium effects in the chemistry.

In Glover et al. (2015; hereafter, Paper I), we presented results from a study of the [C I] emission produced by a model of a turbulent molecular cloud that does not suffer from these inconsistencies. In our simulation, we evolved the chemistry and internal energy of the gas simultaneously with the hydrodynamics, allowing us to capture any influence of the non-isothermal equation of state on the dynamical evolution and to ensure that the chemistry is not evolved for a longer period of time than the dynamics. The cloud that we modeled in Paper I had a solar metallicity, and was illuminated by the standard Draine (1978) ultraviolet (UV) radiation field. We found, in agreement with Offner et al. (2014), that the [C I] emission line was a good tracer of the molecular mass of the cloud.

In the present paper, we extend this study by examining clouds with a range of different metallicities. For each metallicity, we run models with several different values for the strength of the ISRF. Our goal is to understand how well [C I] emission can be used as a tracer of molecular gas in this wider range of systems, and whether it becomes clearly superior to CO at low metallicities. Since clouds in extragalactic systems are typically unresolved or only marginally resolved, our main focus in this study is on how X_{CI} varies as a function of metallicity, radiation field strength and time.

The structure of our paper is as follows. In Section 2, we outline the numerical method used to perform our simulations and to post-process the results. We also give details of the initial conditions that we used for our simulations. In Section 3, we present and discuss our results. Finally, we conclude in Section 4.

2 METHOD

2.1 Hydrodynamical model

To model the chemical, thermal and dynamical evolution of the gas in our model clouds, we use a modified version of the Gadget 2 SPH code (Springel 2005). Our modified version of the code includes a simplified chemical model that follows the abundances of H, H_2 , H^+ , C, C^+ , CO, HCO^+ , He, He^+ , and free electrons (Glover & Mac Low 2007a,b; Nelson & Langer 1999), a detailed cooling function, and a treatment of the effects of attenuation of the interstellar radiation field

¹ <http://www.ita.uni-heidelberg.de/~dullemond/software/radmc-3d/>

(ISRF) based on the TREECOL algorithm (Clark, Glover & Klessen 2012). To model gravitationally collapsing regions that become too small to resolve, we use a sink particle algorithm based on Bate, Bonnell & Price (1995) and Jappsen et al. (2005). The version of the code used here is the same as that used in Paper I, and a more extensive discussion of its capabilities can be found in that paper.

Although our use of a simplified chemical network introduces some uncertainty into our results that would not be present if we used a more extensive network, the impact of this on our predicted C and CO abundances is likely to be small. We showed in an earlier paper (Glover & Clark 2012c) that the simplified chemical network that we use in this study produces comparable results for the C and CO distributions to the larger Glover et al. (2010) network. That network was in turn benchmarked against an extensive model derived from the UMIST astrochemical database (Woodall et al. 2007) and shown to produce results in good agreement with the latter for a range of different physical conditions. In addition, the fact that our results agree well with those of Offner et al. (2014), who make use of a chemical network containing over 200 species and several thousand reactions, also gives us confidence that our use of a simplified network is not a major source of error.

2.2 Post-processing

We construct synthetic emission maps of our simulated clouds in the $^3P_1 \rightarrow ^3P_0$ fine structure line of [C I] (hereafter simply referred to as the [C I] 1 \rightarrow 0 line) and the $J = 1 \rightarrow 0$ line of ^{12}CO using the RADMC-3D radiation transfer code. The region modelled with RADMC-3D is a cubical sub-volume of the cloud, with a side length of 16.2 pc that contains almost all of the CO and neutral atomic carbon present in the model clouds. Before feeding our data to RADMC-3D, we first interpolate it onto a Cartesian grid with a resolution of 256^3 zones. In Paper I we explored the effect of varying this resolution and showed that 256^3 zones was sufficient to fully resolve the [C I] emission.

To compute the level populations required by the code, we used the large velocity gradient (LVG) approximation. The implementation of this approximation within RADMC-3D is described in detail in Shetty et al. (2011a,b). We fixed the velocity resolution of the code at $\Delta v = 0.094 \text{ km s}^{-1}$ and accounted for small-scale unresolved velocity fluctuations by including a microturbulent contribution to the linewidth with size $v_{\text{mturb}} = 0.2 \text{ km s}^{-1}$. However, the values that we derived for the [C I] and CO velocity-integrated intensities are relatively insensitive to these choices.

2.3 Initial conditions

Our default initial conditions in this study are similar to those used in paper I and in several other previous papers (see e.g. Glover & Clark 2012a,b). The cloud mass is $10^4 M_{\odot}$, and the cloud is simulated using two million SPH particles. The resulting mass resolution is $0.5 M_{\odot}$. In paper I, we explored the effects of increasing this resolution, but found that this resulted in only minor differences in the [C I] emission produced by the cloud. The cloud was initially spherical, with a radius of 6.3 pc. The initial H nuclei number density

of the gas was $n_0 = 276 \text{ cm}^{-3}$, within a factor of two of the median value determined for local GMCs by Roman-Duval et al. (2010). The initial gas temperature was $T_{\text{gas}} = 20 \text{ K}$ and the initial dust temperature was $T_{\text{dust}} = 10 \text{ K}$.²

The velocity field of the gas in the clouds was constructed as a Gaussian random field, with a power spectrum $P(k) \propto k^{-4}$, where k is the wavenumber. The amplitude of the velocity fluctuations was constrained to yield an initial RMS velocity of $v_{\text{rms}} = 2.8 \text{ km s}^{-1}$. This value was chosen so that the initial kinetic energy of the cloud was equal to its gravitational binding energy. The velocity field was then allowed to evolve during the simulation without any further kinetic energy input. The cloud was simulated using vacuum boundary conditions, but the artificial “evaporation” of material from the edge of the cloud was prevented by the application of an external pressure term (Benz 1990).

We performed a series of simulations using these initial conditions, and varying the metallicity of the gas and the strength of the imposed radiation field. The values used in the different simulations are summarized in Table 1. In our solar metallicity simulations, the total abundances of carbon and oxygen relative to hydrogen were taken to be $x_{\text{C}} = 1.4 \times 10^{-4}$ and $x_{\text{O}} = 3.2 \times 10^{-4}$, respectively (Sembach et al. 2000). In the lower metallicity simulations, these values were scaled by a factor Z/Z_{\odot} . In most of our simulations, we also assumed that the dust-to-gas ratio \mathcal{D} scaled as Z/Z_{\odot} . However, there is some observational evidence that it actually falls off more rapidly as the metallicity decreases (e.g. Galametz et al. 2011; Herrera-Camus et al. 2012; Rémy-Ruyer et al. 2014), and so we also performed three simulations (Z05-G1-D0375, Z02-G1-D01 and Z01-G1-D001) in which we adopted smaller dust-to-gas ratios. For simplicity, we neglect any effects arising due to changes in the size distribution or composition of the dust as we change the metallicity and dust-to-gas ratio. In all of our simulations, the oxygen and hydrogen were assumed to begin in neutral atomic form, and the carbon was assumed to start as C^+ .

The spectral shape of our adopted interstellar radiation field follows Draine (1978) in the ultraviolet and Mathis, Mezger & Panagia (1983) at longer wavelengths. We consider several different radiation field strengths, quantified by the parameter G_0 which is normalized so that $G_0 = 1$ corresponds to the Draine (1978) radiation field. In our TREECOL-based treatment of the attenuation of the radiation field, we used a total of 48 pixels to represent the angular variation of the radiation field around each SPH particle. In paper I, we verified that this was sufficient to yield well-converged results. In most of our runs, we adopted a cosmic ray ionization rate for atomic hydrogen given by $\zeta_{\text{H}} = \zeta_{\text{H},0} = 10^{-17} \text{ s}^{-1}$. However, we also carried out a few simulations with larger values of ζ_{H} . Cosmic ray ionization rates for H_2 , CO etc. were computed by scaling the H ionization rates, as described in Glover & Clark (2012b).

Table 1. List of simulations

ID	Z/Z_{\odot}	G_0	$\zeta_{\text{H}}/\zeta_{\text{H},0}$	Notes
Z1-G1	1.0	1	1	
Z1-G10	1.0	10	1	
Z1-G100	1.0	100	1	
Z05-G1	0.5	1	1	
Z05-G10	0.5	10	1	
Z05-G100	0.5	100	1	
Z03-G1	0.3	1	1	
Z03-G10	0.3	10	1	
Z03-G100	0.3	100	1	
Z02-G1	0.2	1	1	
Z02-G10	0.2	10	1	
Z02-G100	0.2	100	1	
Z01-G1	0.1	1	1	
Z01-G10	0.1	10	1	
Z01-G100	0.1	100	1	
Z003-G1	0.03	1	1	
Z003-G10	0.03	10	1	
Z003-G100	0.03	100	1	
Z05-G1-D0375	0.5	1	1	$\mathcal{D} = 0.375 \mathcal{D}_{\odot}$
Z02-G1-D01	0.2	1	1	$\mathcal{D} = 0.1 \mathcal{D}_{\odot}$
Z01-G1-D001	0.1	1	1	$\mathcal{D} = 0.01 \mathcal{D}_{\odot}$
Z1-G10-CR10	1.0	10	10	
Z1-G100-CR100	1.0	100	100	
Z03-G10-CR10	0.3	10	10	
Z03-G100-CR100	0.3	100	100	
Z01-G10-CR10	0.1	10	10	
Z01-G100-CR100	0.1	100	100	

\mathcal{D} denotes the dust-to-gas ratio, with \mathcal{D}_{\odot} being the value in the local ISM. G_0 is the strength of the ISRF relative to Draine (1978) and Mathis, Mezger & Panagia (1983).

3 RESULTS

3.1 The [C I]-to- H_2 conversion factor at the onset of star formation

In Paper I we showed that in a typical turbulent Galactic cloud, the integrated intensity of the [C I] $1 \rightarrow 0$ line ($W_{\text{CI},1-0}$) scales linearly with the H_2 column density (N_{H_2}) only over a limited range of H_2 column densities. At high column densities, the correlation breaks down because the $1 \rightarrow 0$ line becomes optically thick, while at low column densities, the breakdown reflects the fact that most of the carbon in regions of low extinction is photoionized to C^+ by the external radiation field. Observations of [C I] in Galactic molecular clouds recover similar behaviour (see e.g. Beuther et al. 2014). In the present paper, we show that increasing the radiation field strength and/or decreasing the metallicity does not substantially change this basic conclusion. This is illustrated in Figure 1, where we show two examples of the relationship between $W_{\text{CI},1-0}$ and N_{H_2} , taken from runs Z1-G10 and Z02-G1. In both cases, the values shown are for a

² Note that since T_{gas} and T_{dust} rapidly adjust to close to their thermal equilibrium values following the beginning of the simulations, our results do not depend on these starting values.

Table 2. Onset of star formation in each simulation

ID	t_{SF} (Myr)
Z1-G1	1.98
Z1-G10	2.17
Z1-G100	2.05
Z05-G1	2.43
Z05-G10	2.58
Z05-G100	2.79
Z03-G1	2.72
Z03-G10	2.86
Z03-G100	3.24
Z02-G1	2.81
Z02-G10	2.97
Z02-G100	3.59
Z01-G1	2.95
Z01-G10	3.22
Z01-G100	4.25
Z003-G1	3.20
Z003-G10	3.61
Z003-G100	4.81
Z05-G1-D0375	2.54
Z02-G1-D01	2.93
Z01-G1-D001	2.97
Z1-G10-CR10	2.17
Z1-G100-CR100	2.03
Z03-G10-CR10	2.88
Z03-G100-CR100	2.58
Z01-G10-CR10	3.25
Z01-G100-CR100	—

time immediately before the onset of star formation, $t = t_{\text{SF}}$. The actual physical time that this corresponds to for each cloud is listed in Table 2. We see that in both cases, there is an approximately linear correlation between $W_{\text{CI},1-0}$ and N_{H_2} only over a relatively narrow range in H_2 column densities. At low column densities, $W_{\text{CI},1-0}$ falls off rapidly with decreasing N_{H_2} , reflecting the fact that most of the carbon is photoionized to C^+ in regions with low dust extinction. At high column densities, on the other hand, the correlation between $W_{\text{CI},1-0}$ and N_{H_2} becomes sub-linear because the [C I] $1 \rightarrow 0$ line becomes optically thick. Moreover, even in the range of H_2 column densities where the mean value of $W_{\text{CI},1-0}$ does scale approximately linearly with N_{H_2} , we see that there is considerable scatter.

It is clear from this that on small scales, there is no unique [C I]-to- H_2 conversion factor. Instead, we would expect the conversion factor to vary significantly with position within the cloud, similar to the behaviour that we find for X_{CO} (see e.g. Pineda, Caselli & Goodman 2008; Shetty et al. 2011a,b; Lee et al. 2014). A more interesting quantity to examine is therefore the mean [C I]-to- H_2 conversion factor for the entire cloud. We define this as

$$X_{\text{CI}} \equiv \frac{\langle N_{\text{H}_2} \rangle}{\langle W_{\text{CI},1-0} \rangle}, \quad (2)$$

where the angle brackets denote the fact that we are averaging over the projected spatial extent of the cloud. We define X_{CI} for the cloud in this way, rather than by computing its

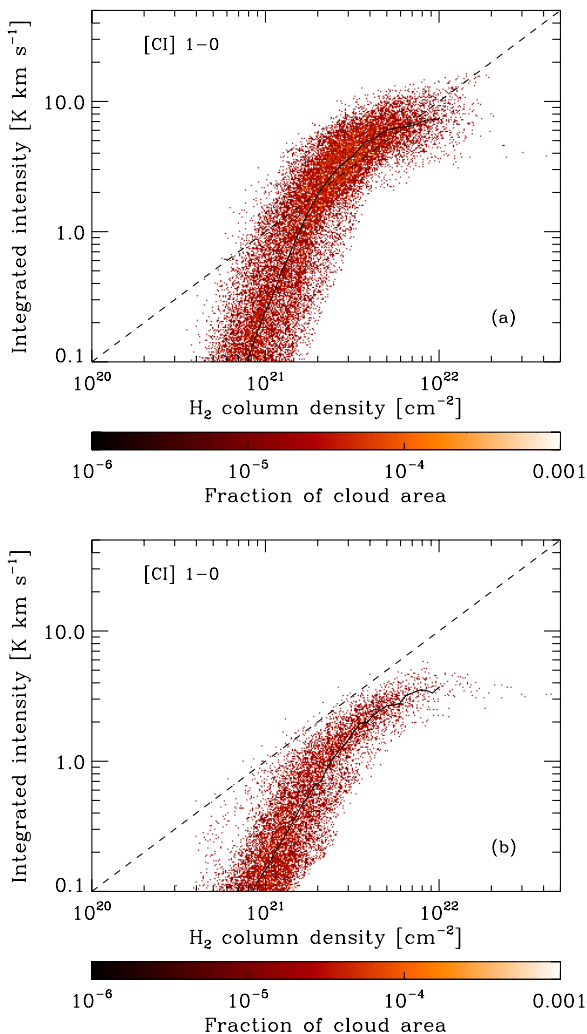


Figure 1. (a) Two-dimensional PDF of the integrated intensity of the [C I] $1 \rightarrow 0$ line, plotted as a function of the H_2 column density, N_{H_2} , for run Z1-G10 at $t = t_{SF}$. The dashed line indicates a linear relationship between $W_{CI,1-0}$ and N_{H_2} and is included to help guide the eye. The solid line shows the geometric mean of $W_{CI,1-0}$ as a function of N_{H_2} . The points are colour-coded according to the fraction of the total cloud area that they represent. (b) As (a), but for run Z02-G1 at $t = t_{SF}$.

value for each individual pixel and then averaging, for two reasons. First, this better reflects what we are actually doing when we make observations of unresolved molecular clouds and hence measure only the total emission rather than its spatial distribution. Second, this procedure allows us to deal sensibly with lines-of-sight that have H_2 without any significant associated [C I] emission.

When computing $\langle N_{H_2} \rangle$ and $\langle W_{CI,1-0} \rangle$, we include all of the pixels in our projections that have non-zero H_2 column densities. However, we note that this is not the only possible way in which to compute ‘average’ H_2 column densities and [C I] integrated intensities for the simulated clouds. A commonly-used alternative method involves defining some minimum column density or intensity threshold, and then only averaging over the set of pixels with values above this threshold (see e.g. Clark & Glover 2015, or Szücs et al.,

in prep.) This procedure better matches what is done in resolved observations of clouds (e.g. Lee et al. 2014), while the procedure that we adopt is more appropriate if the clouds are unresolved.

In Figure 2a, we show how X_{CI} varies as a function of metallicity and radiation field strength for our simulated clouds. Once again, we show the results for $t = t_{SF}$. The values of X_{CI} shown in this figure are given in terms of the canonical Galactic CO-to- H_2 conversion factor, $X_{CO,MW}$.

Two points are immediately obvious. First, at solar metallicity, X_{CI} is significantly larger than $X_{CO,MW}$. In run Z1-G1, we recover a value of $X_{CI} = 8.8 \times 10^{20} \text{ cm}^{-2} \text{ K}^{-1} \text{ km}^{-1} \text{ s}$, within 25% of the value computed by Offner et al. (2014) for a somewhat denser cloud. This is more than a factor of 4 larger than $X_{CO,MW}$, and roughly three times larger than the value of X_{CO} that we recover for the same simulated cloud (see Figure 2b). Increasing the strength of the ISRF by a factor of 10–100 increases X_{CI} by around 30–50%, but also increases X_{CO} by roughly the same amount. Therefore, at solar metallicity and at this point in the clouds’ evolution, there does not appear to be a compelling reason to prefer [C I] over CO as a tracer of the total cloud mass.

Second, Figure 2a demonstrates that X_{CI} systematically increases as we reduce the metallicity of the gas, with a scaling that is close to $X_{CI} \propto Z^{-1}$ in the $G_0 = 1$ runs. In the runs with stronger radiation fields, we see a slightly steeper scaling for metallicities in the range $0.2 < Z/Z_\odot < 1.0$, which then flattens as we move to even lower metallicities.

For comparison, we illustrate in Figure 2b how the value of X_{CO} that we measure at the onset of star formation varies with metallicity. As in the case of X_{CI} , we see that at $Z \geq 0.2 Z_\odot$, X_{CO} increases as the metallicity decreases, with a dependence that again scales roughly as Z^{-1} . At lower metallicities, the behaviour becomes more complicated. When $G_0 = 1$, X_{CO} continues to increase with decreasing metallicity, but in the $G_0 = 10$ and $G_0 = 100$ runs we find instead that X_{CO} remains constant or even decreases with decreasing Z . This occurs because in these conditions, the total CO emission of the cloud becomes dominated by the contribution from a single dense, compact, gravitationally-collapsing clump (see Figure 3). The high column density of the gas in this clump provides effective shielding for the CO even when the metallicity is very low, and allows the gas to build up a large CO column density within the clump. Consequently, the CO emission from the clump becomes optically thick, at which point it becomes only weakly sensitive to the fractional abundance of CO within the dense gas. As a result, the mean value of the ^{12}CO integrated intensity, $\langle W_{CO} \rangle$, which varies strongly with metallicity at high Z , starts to vary only weakly with metallicity once we reach this clump-dominated regime. At the same time, however, the H_2 content of the cloud still decreases substantially with decreasing metallicity even once we reach this clump-dominated regime, since even at the lowest metallicities, much of the H_2 is still located outside of the dense clump.

The results of our comparison show that at this point in the evolution of the cloud, the cloud-averaged CO emission remains a better tracer of the molecular mass than the cloud-averaged [C I] emission, even at metallicities as low as $Z = 0.03 Z_\odot$. This can be seen more easily if we plot the

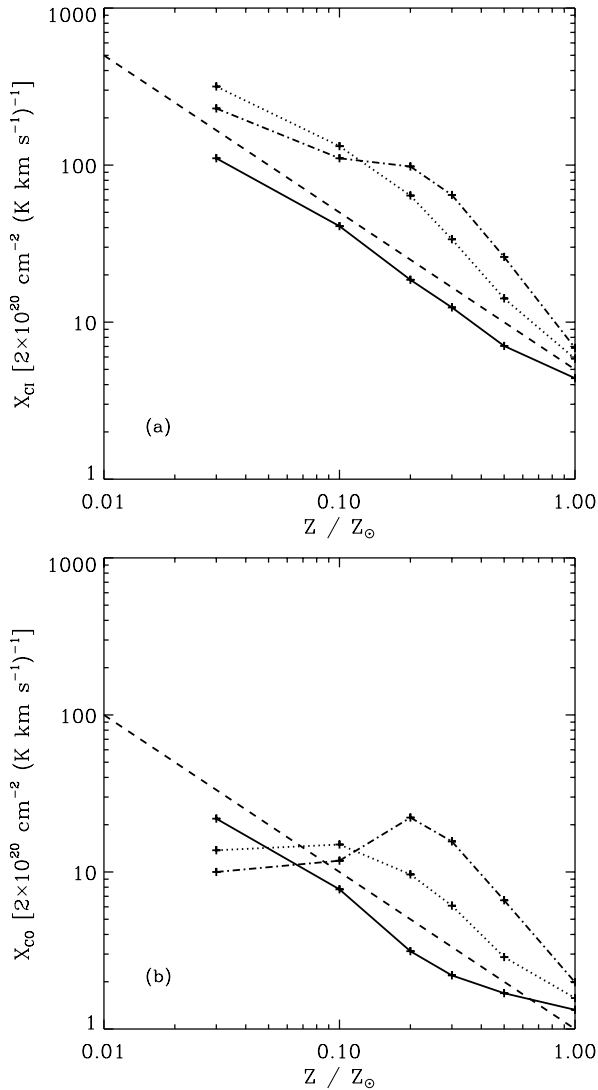


Figure 2. (a) [C I]-to-H₂ conversion factor at $t = t_{\text{SF}}$, computed for the [C I] 609 μm line, and plotted in units of the Galactic CO-to-H₂ conversion factor ($X_{\text{CO,MW}} = 2 \times 10^{20} \text{ cm}^{-2} (\text{K km/s})^{-1}$) for a range of different metallicities and radiation field strengths. We show results for radiation field strengths $G_0 = 1$ (solid line), $G_0 = 10$ (dotted line) and $G_0 = 100$ (dash-dotted line). The dashed line indicates a slope of Z^{-1} and is included merely to guide the eye. (b) As (a), but for the CO-to-H₂ conversion factor, X_{CO} .

ratio of X_{CO} to X_{CI} , which is the same as the ratio of the cloud-averaged [C I] and CO integrated intensities. This is shown in Figure 4. We see that in clouds at the onset of star formation, $\langle W_{\text{CI}} \rangle / \langle W_{\text{CO}} \rangle$ decreases as we decrease the metallicity, although the dependence is fairly weak: an order of magnitude drop in Z leads to a decrease in the intensity ratio of no more than a factor of two. We also see that except at the very lowest metallicity that we study, $\langle W_{\text{CI}} \rangle / \langle W_{\text{CO}} \rangle$ is highly insensitive to the value of G_0 .

3.2 Time evolution of X_{CI} and X_{CO}

In the previous section, we examined the behaviour of X_{CI} and X_{CO} in the case where the gas has already collapsed

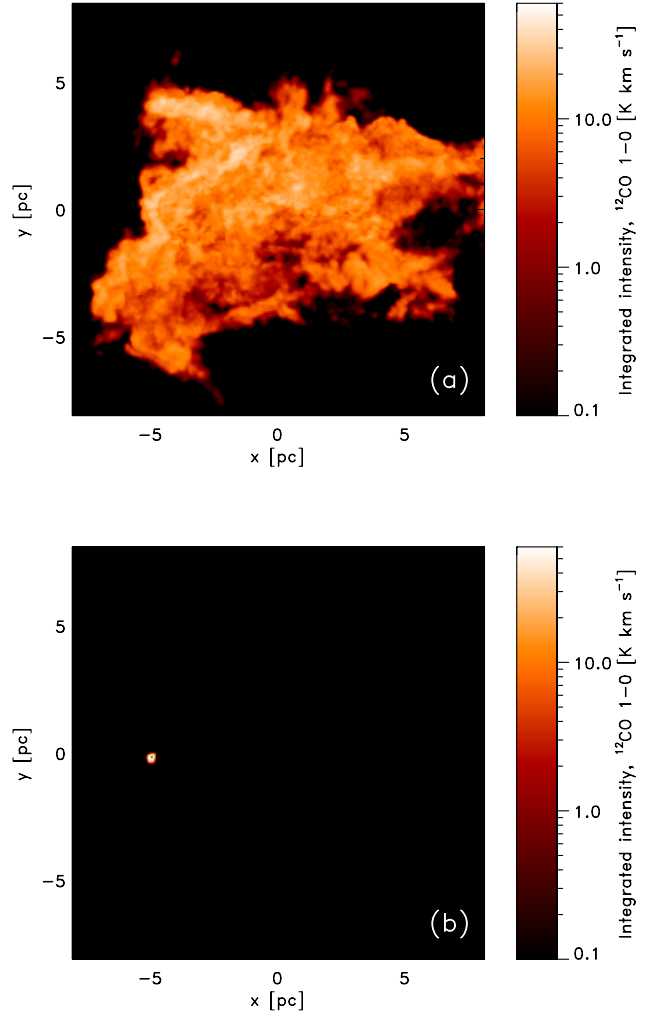


Figure 3. (a) Map of the integrated intensity of the $J = 1 \rightarrow 0$ transition of ^{12}CO in run Z1-G1 at time $t = t_{\text{SF}}$. (b) As (a), but for run Z01-G100.

and started forming stars, and showed that in this case, CO is a superior tracer of the molecular mass, at least for the range of metallicities and UV field strengths considered here. However, it does not immediately follow that CO will be a superior tracer of H₂ at all times during the evolution of the cloud. As we have already seen, at low metallicity the bulk of the CO emission produced by the cloud comes from between one and a few dense, compact, collapsing clumps (see also Glover & Clark 2012b, who report similar results). These clumps have higher volume densities and higher extinctions than the bulk of the cloud, and hence are the regions in which CO is best able to resist photodissociation. However, the dynamical timescale on which these clumps evolve is relatively short: they will either collapse on a free-fall timescale ($t_{\text{ff}} \simeq 0.5 \text{ Myr}$ for clumps with a mean density $n \sim 10^4 \text{ cm}^{-3}$, or even shorter at higher densities), or will be disrupted by turbulence on a similar timescale. This prompts us to ask how X_{CI} and X_{CO} evolve as a function of time: do we find larger values at earlier times, when these dense clumps have not yet formed?

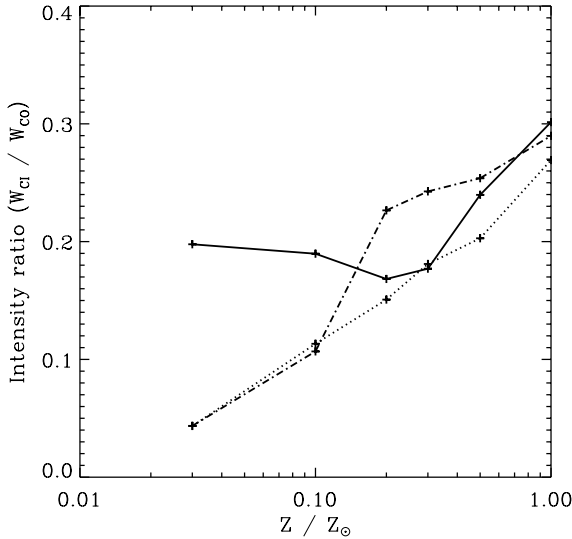


Figure 4. Ratio of the mean integrated intensities (in K km s^{-1}) of the [C I] 609 μm line ($\langle W_{\text{CI}} \rangle$) and the $^{12}\text{CO } J = 1 \rightarrow 0$ line ($\langle W_{\text{CO}} \rangle$), computed at $t = t_{\text{SF}}$ and plotted as a function of metallicity. We show results for radiation field strengths $G_0 = 1$ (solid line), $G_0 = 10$ (dotted line) and $G_0 = 100$ (dash-dotted line).

To investigate this, we have calculated X_{CI} and X_{CO} for each of our clouds at a time $t = t_{\text{SF}} - 1$ Myr. The results are plotted in Figure 5. We see that when $G_0 = 1$, the values of X_{CI} that we measure at $t = t_{\text{SF}} - 1$ Myr are similar to or smaller than those that we measure at $t = t_{\text{SF}}$. In other words, in these conditions, [C I] emission remains a good tracer of the molecular mass of the cloud even prior to the onset of gravitational collapse. The same is true in the runs with $G_0 = 10$ and 100 at solar metallicity, but not at lower metallicities, where we find a much steeper increase in X_{CI} with decreasing Z than we did in the previous section. That said, the actual increase in the values of X_{CI} relative to those in the $t = t_{\text{SF}}$ case remains relatively modest: at most, we see increases of around a factor of a few.

The story is very different in the case of CO. At solar metallicity, much of the CO emission comes from gas with a number density of a few thousand cm^{-3} . Regions with this density are found throughout the cloud (see e.g. Figure 5 in Glover & Clark 2012b) and most of this gas is not self-gravitating. Individual CO-bright regions are formed and destroyed by the action of the turbulence, but the total amount of gas in these regions does not vary much. Consequently, X_{CO} does not vary strongly with time. At much lower metallicities, however, dense, self-gravitating clumps dominate the total emission, and the value of X_{CO} becomes highly sensitive to the evolutionary state of these clumps. In this case, the values that we measure for X_{CO} at $t = t_{\text{SF}} - 1$ Myr are much, much larger than those at $t = t_{\text{SF}}$.

This point is further emphasized if we look at the [C I]/CO integrated intensity ratio at the same time (Figure 6). At metallicities close to solar, the ratio of the [C I] and CO integrated intensities at this point in the cloud’s evolution is around 0.5 to 0.6 (for values expressed in terms of K km s^{-1}), somewhat larger than at $t = t_{\text{SF}}$, but of the same order of magnitude. At lower metallicities, however, the ratio increases dramatically as the diffuse CO emission

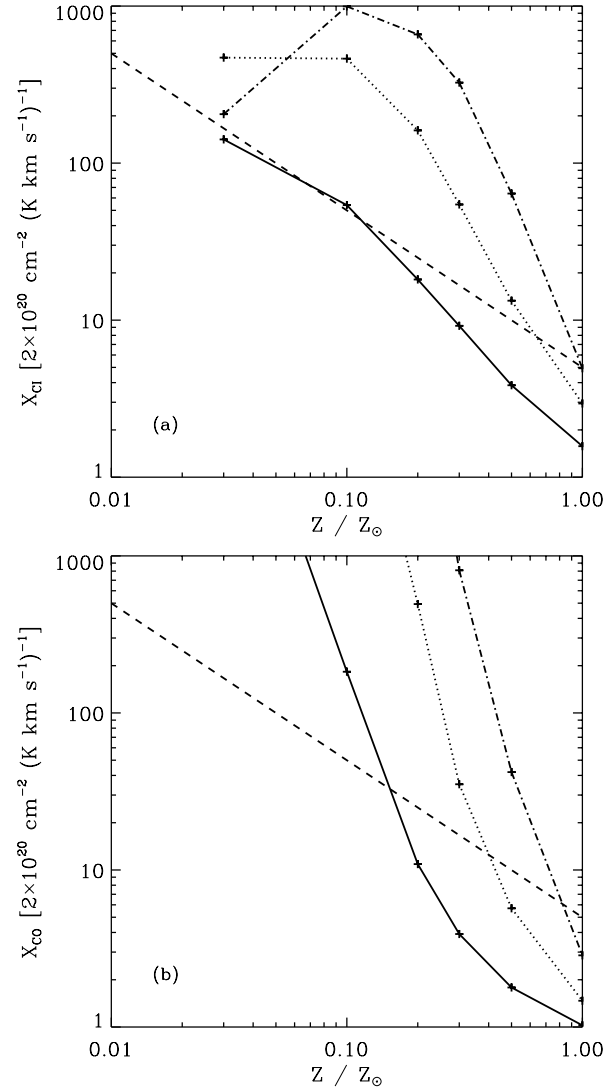


Figure 5. (a) As Figure 2a, but showing values of X_{CI} computed at $t = t_{\text{SF}} - 1$ Myr. (b) As (a), but for X_{CO} .

vanishes. When $G_0 = 1$, this sharp increase in the [C I]/CO intensity ratio occurs at a metallicity of around $0.1 Z_{\odot}$, but increasing G_0 leads to this change of behaviour happening at higher metallicity, owing to the more effective destruction of the diffuse CO in runs with a higher radiation field strength.

In Figure 7a, we explore in more detail how X_{CI} and X_{CO} evolve with time in several representative runs. In run Z1-G1, X_{CI} rises gradually over time as the cloud collapses and an increasing fraction of the available carbon is converted into CO. In run Z02-G10, on the other hand, the collapse of the cloud leads to a decrease in X_{CI} , as in this case, the increased conversion of C^+ to C is more important than the conversion of C to CO. Finally, in run Z003-G100, there is no clear trend in the evolution of X_{CI} with time. Importantly, we see that in no case does X_{CI} vary by more than a factor of a few over the time period examined, which corresponds to roughly half a free-fall time.

If we now look at the evolution of X_{CO} in the same three runs over the same period of time (Figure 7b), we

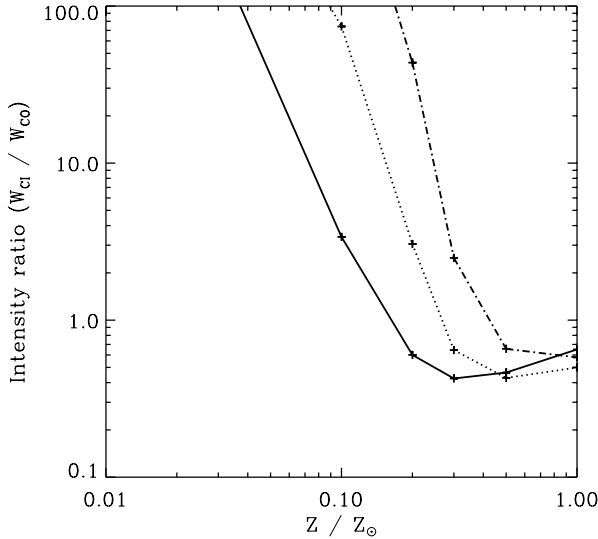


Figure 6. As Figure 4, but for $t = t_{\text{SF}} - 1$ Myr. We show results for radiation field strengths $G_0 = 1$ (solid line), $G_0 = 10$ (dotted line) and $G_0 = 100$ (dash-dotted line). Note the difference in vertical scale between this figure and Figure 4.

see that the behaviour is very different. In run Z1-G1, the dense clumps and filaments created by the turbulence provide enough shielding to allow significant quantities of CO to form even prior to the onset of run-away gravitational collapse. Consequently, the CO content of the cloud does not change substantially over time and X_{CO} remains approximately constant.

In run Z02-G10, on the other hand, the combination of the lower dust extinction and higher radiation field strength mean that the over-dense structures created by the turbulence alone contain little CO. In this case, it is the gravitational collapse of some of these structures that triggers a substantial increase in the CO luminosity of the cloud. The result is that in this run, X_{CO} evolves strongly over time, decreasing by almost a factor of 100 over the 1.5 Myr period shown here.

Finally, we see that in run Z003-G100, the time-dependence of X_{CO} becomes even more extreme. In this run, CO forms only at very high densities, shortly before the onset of star formation, and so X_{CO} rapidly changes from being orders of magnitude larger than the Galactic value at $t \ll t_{\text{SF}}$ to only 5–10 times larger than the Galactic value at $t \sim t_{\text{SF}}$ and later times.

3.3 Dependence of W_{C1} and W_{CO} on extinction

To help us understand why X_{C1} is much less time dependent than X_{CO} in low metallicity clouds, it is useful to look at how the integrated intensities of the [C I] 609 μm line and the CO $J = 1 \rightarrow 0$ line depend on the line-of-sight visual extinction of the gas and how this dependence changes as we vary the metallicity. In Figure 8a, we show a cumulative plot of the fraction of the total [C I] emission coming from lines-of-sight at or below the specified visual extinction for a number of different simulations that cover the full range of metallicities that we examine in this paper. In each case, the curves correspond to the state of the cloud at $t = t_{\text{SF}}$.

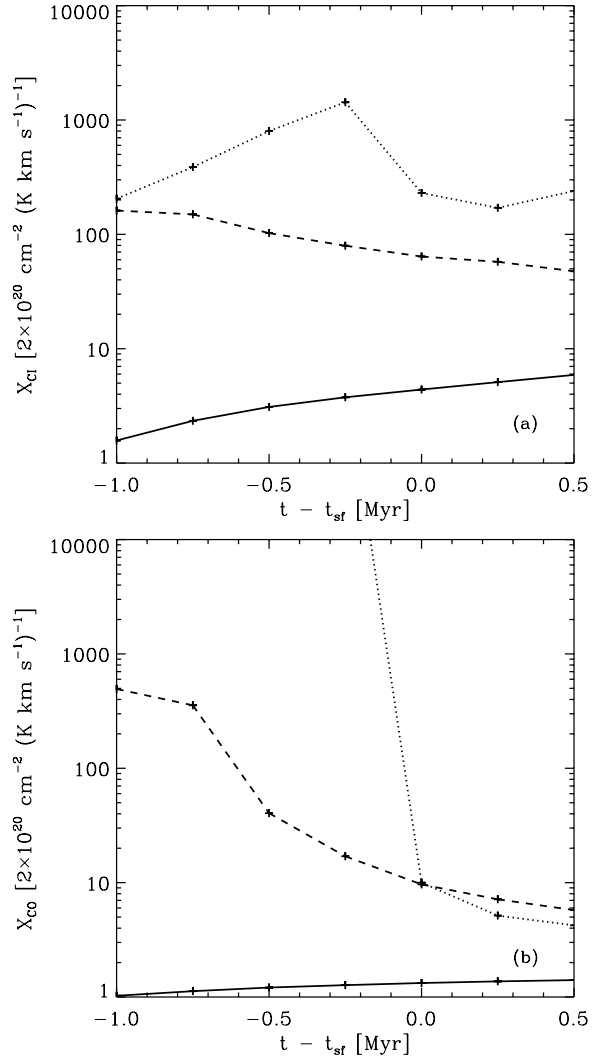


Figure 7. (a) Evolution with time of X_{C1} in runs Z1-G1 (solid line), Z02-G10 (dashed line) and Z003-G100 (dotted line). (b) As (a), but showing the evolution with time of X_{CO} .

In Figure 8b, we show a similar plot for the CO $J = 1 \rightarrow 0$ emission in the same set of simulations.

We see in the solar metallicity run, almost all of the [C I] emission is confined to lines-of-sight with $1 < A_V < 10$, with roughly 50% coming from the narrower range $2.5 < A_V < 5$. However, as we decrease the metallicity, the range of extinctions occupied by the lines-of-sight producing most of the [C I] emission shifts to systematically lower values, so that by the time we reach the 0.03 Z_{\odot} run, almost all of the emission is coming from gas with $A_V < 1$. The amount by which the curve shifts from run to run roughly corresponds to the change in the dust-to-gas ratio, which is consistent with the same range of gas column densities dominating the emission in each case, regardless of the dust-to-gas ratio. This range of column densities extends from a few times 10^{21} cm^{-2} to $\sim 10^{22} \text{ cm}^{-2}$, and it is important to note that the mean H nuclei column density of the cloud at $t = 0$, which is approximately $\langle N_{\text{H}} \rangle_{\text{init}} \simeq 7 \times 10^{21} \text{ cm}^{-2}$, lies in the middle of this range. It is therefore not surprising that the

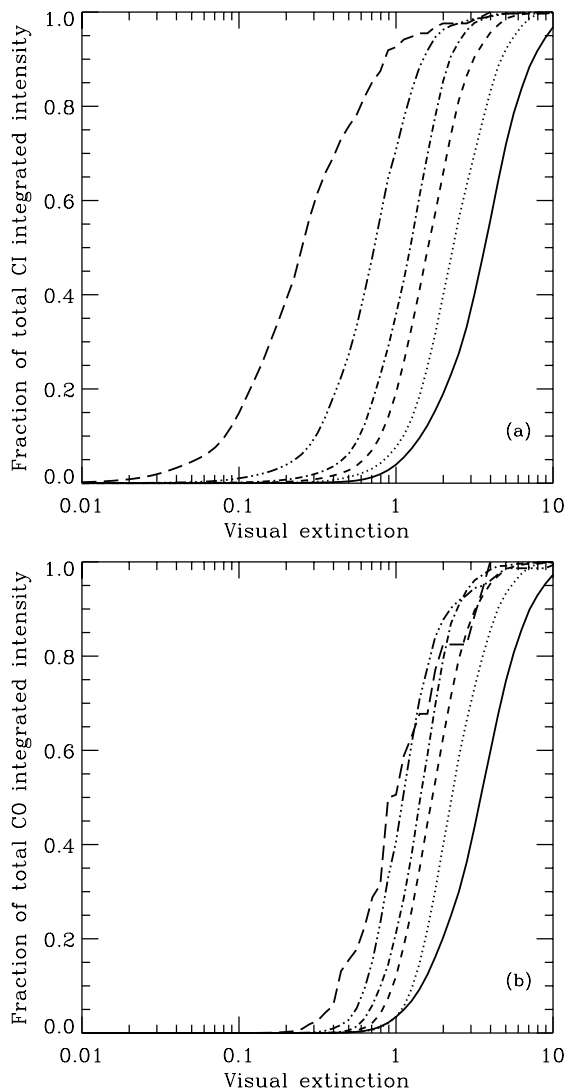


Figure 8. (a) Fraction of the total [C I] emission from the simulated clouds coming from lines of sight with values of A_V at or below the specified value, measured at $t = t_{\text{SF}}$. Results are plotted for runs Z1-G1 (solid), Z05-G1 (dotted), Z03-G1 (dashed), Z02-G1 (dot-dashed), Z01-G1 (dot-dot-dot-dashed) and Z003-G1 (long-dashed). (b) As (a), but for the total $^{12}\text{CO } J = 1 \rightarrow 0$ emission.

clouds are bright in [C I] right from the start of the simulation, and hence that X_{CI} does not vary strongly with time.

In the case of CO, however, we see quite different behaviour, as Figure 8b demonstrates. In run Z1-G1, most of the CO emission is produced by lines of sight with $2 < A_V < 5$, similar to the behaviour of the [C I] emission. As we decrease the metallicity, we again find that the range of extinctions responsible for producing most of the emission shifts to lower values. However, in this case, the lines shift by a much smaller amount: a factor of 30 change in metallicity and dust-to-gas ratio shifts the curves by no more than around a factor of three. This means that the range of gas column densities that dominate the total CO emission shifts to higher values as we decrease the metallicity. For example, in run Z01-G1, around 50% of the total

CO $J = 1 \rightarrow 0$ emission is produced by lines-of-sight with $A_V > 1$, corresponding to $N_{\text{H}} \simeq 2 \times 10^{22} \text{ cm}^{-2}$.

This behaviour provides a simple explanation for the strong time dependence that we see in X_{CO} at low metallicities. In our low metallicity clouds, the column density required to provide sufficient dust shielding to allow CO to form in significant amounts is much higher than the mean cloud column density. We know that in clouds dominated by turbulence, the column density PDF is log-normal, with a typical dispersion around the mean column density of no more than a factor of two in clouds in which the turbulence is primarily solenoidal in nature (see e.g. Federrath et al. 2010; Burkhart & Lazarian 2012; Abreu-Vicente et al. 2015). Consequently, in turbulence-dominated clouds prior to the onset of gravitational collapse, there are few or no lines-of-sight associated with bright CO emission. It follows from this that the mean CO brightness of the cloud is very small, and hence that X_{CO} is very large, since many of these clouds still contain significant amounts of H_2 . However, once runaway gravitational collapse begins, the column density PDF typically develops a pronounced power-law tail at high column densities (see e.g. Klessen 2000; Kainulainen et al. 2009; Schneider et al. 2015). This increases the number of lines-of-sight that have high extinctions and hence significant CO brightnesses. The result is a dramatic increase in the mean CO brightness of the cloud, which drives a dramatic decrease in X_{CO} . Note that we do not see this behaviour in high metallicity clouds because in that case, the mean cloud column density already lies in the range of column densities for which we find bright CO emission. Therefore, in this case, the cloud is CO-bright prior to the onset of runaway gravitational collapse, and so X_{CO} does not vary strongly with time.

3.4 Effect of varying the dust-to-gas ratio

In most of our simulations, we assume that the dust-to-gas ratio \mathcal{D} is linearly proportional to the metallicity Z/Z_{\odot} . Observationally, this seems to be a reasonable assumption for metal-rich galaxies like our own Milky Way (Sandstrom et al. 2013). However, there is growing evidence that in metal-poor systems, such as dwarf galaxies, the dust-to-gas ratio becomes a much steeper function of the gas-phase metallicity (see e.g. Galametz et al. 2011; Herrera-Camus et al. 2012; Rémy-Ruyer et al. 2014). It is therefore useful to examine what effect this steeper dependence of \mathcal{D} on Z may have on our results for X_{CI} and X_{CO} .

We have therefore performed three additional simulations in which the dust-to-gas ratio was not simply scaled with Z/Z_{\odot} . In run Z05-G1-D0375, we adopted a gas-phase metallicity of $Z = 0.5 Z_{\odot}$ and a dust-to-gas ratio of $\mathcal{D} = 0.375 \mathcal{D}_{\odot}$. In run Z02-G1-D01, we adopted a gas-phase metallicity $Z = 0.2 Z_{\odot}$ and a dust-to-gas ratio $\mathcal{D} = 0.1 \mathcal{D}_{\odot}$. Finally, in run Z01-G1-D001, we adopted a gas-phase metallicity $Z = 0.1 Z_{\odot}$ and a dust-to-gas ratio $\mathcal{D} = 0.01 \mathcal{D}_{\odot}$. The values in the first of these runs were chosen to be a good match for the gas-phase metallicity and dust-to-gas ratio in the Large Magellanic Cloud (Gordon et al. 2014), while the values in the other two runs were chosen to be consistent with the relationship between metallicity and dust-to-gas ratio inferred by Rémy-Ruyer et al. (2014).

In Table 3, we list the values of X_{CI} and X_{CO} in these

Table 3. Comparison of X_{CI} and X_{CO} in runs with low and standard dust-to-gas ratios

ID	$X_{\text{CI}}(t_1)$	$X_{\text{CO}}(t_1)$	$X_{\text{CI}}(t_{\text{SF}})$	$X_{\text{CO}}(t_{\text{SF}})$
Z05-G1-D0375	4.21	2.21	7.15	1.76
Z05-G1	3.85	1.79	7.05	1.69
Z02-G1-D01	18.7	35.1	16.2	3.57
Z02-G1	18.2	10.9	18.6	3.13
Z01-G1-D001	9.32	3420	10.5	6.15
Z01-G1	54.0	183	40.9	7.75

X_{CI} and X_{CO} are given in units of the Galactic CO-to- H_2 conversion factor $X_{\text{CO},\text{MW}}$ (see Eq. 1). Values are shown for t_{SF} and $t_1 \equiv t_{\text{SF}} - 1$ Myr.

runs at t_{SF} and $t_1 \equiv t_{\text{SF}} - 1$ Myr. For comparison, we also list the values of X_{CI} and X_{CO} at the same times in runs with the same metallicity and radiation field strength but with a dust-to-gas ratio scaled linearly with metallicity.

We see from the table that in run Z05-G1-D0375, the lower dust-to-gas ratio has only a small effect on the outcome of the simulations. We recover systematically higher values of X_{CI} and X_{CO} than in run Z05-G1, but only by a small amount: around 10-20% at t_1 , and less than 5% at $t = t_{\text{SF}}$.

In run Z02-G1-D01, we also find only minor differences compared to run Z02-G1 if we look at X_{CI} or at the value of X_{CO} measured at t_{SF} . However, we see that there is a much larger difference in X_{CO} at earlier times: at $t = t_1$, it is roughly three times larger in run Z02-G1-D01 than in run Z02-G1. This difference in behaviour is again a consequence of the fact that at $t = t_1$, the CO emission from this cloud is dominated by emission from diffuse gas, while at $t = t_{\text{SF}}$, it is dominated by emission from a single dense core. The visual extinction of the dense core is sufficiently high that even if we decrease the dust-to-gas ratio by a factor of two, it still remains well-shielded, allowing CO to resist photodissociation. Consequently, the change in \mathcal{D} does not have a strong influence on the value of X_{CO} that we recover at this point in the evolution of the cloud. At earlier times, however, most of the CO emission is produced by gas with a relatively low visual extinction. The amount of CO that can survive in this gas is much more sensitive to changes in A_V , and hence to change in the dust-to-gas ratio, and so it is not surprising that in this regime, X_{CO} is highly sensitive to the value of \mathcal{D} .

Finally, in run Z01-G1-D001, we see that the substantial reduction in \mathcal{D} that is inferred for very low metallicity systems leads to significant changes in both X_{CI} and X_{CO} . Reducing \mathcal{D} by a large amount – a factor of ten in this case – has two main effects. First, it significantly reduces the amount of H_2 formed in the cloud, since the H_2 formation rate is proportional to \mathcal{D} . Second, it reduces the amount of dust shielding, which decreases the equilibrium abundances of both atomic carbon and CO. In the case of [C I], the former effect dominates: although the mean [C I] integrated intensity decreases, the H_2 column density decreases by a much larger factor, and so X_{CI} decreases. For CO at early times (i.e. prior to runaway gravitational collapse), the reduction in shielding dominates instead. The CO abundance and CO integrated brightness both decrease by a much larger factor than the H_2 column density, and so X_{CO} increases signifi-

cantly. Finally, at $t = t_{\text{SF}}$, when the total CO emission of the cloud is dominated by the contribution from the gravitationally collapsing core, X_{CO} becomes largely independent of \mathcal{D} , decreasing by only 20% for a factor of ten decrease in \mathcal{D} .

3.5 Effect of varying the cosmic ray ionization rate

In most of the simulations presented in this paper, we have kept the cosmic ray ionization rate of atomic hydrogen fixed at its default value of $\zeta_{\text{H},0} = 10^{-17} \text{ s}^{-1}$, even when varying the strength of the interstellar radiation field. We have done this in order to allow us to focus solely on the effect of varying one parameter at a time. However, it is likely that this is not a good approximation for the behaviour of real star-forming systems. The low energy cosmic rays that make the dominant contribution to ζ_{H} are believed to be produced by Fermi acceleration in supernova remnants. Therefore, the cosmic ray energy density should scale linearly with the supernova rate, provided that the mean time between supernovae is shorter than the timescale on which the cosmic rays escape from the galaxy. The supernova rate in turn depends on the star formation rate, averaged on a 10–20 Myr timescale, and so it is reasonable to assume that the cosmic ray energy density, and hence the cosmic ray ionization rate, should scale linearly with the star formation rate (see e.g. Papadopoulos 2010; Papadopoulos et al. 2011). The ultraviolet portion of the ISRF that is responsible for the photodissociation of H_2 and CO and the photoionization of atomic carbon is dominated by emission from massive stars, and so should also scale linearly with the star formation rate. Therefore, in a real star-forming system, it is likely that increases in G_0 are associated with comparable increases in ζ_{H} .

To investigate the effect that this has on the relative importance of [C I] and CO as tracers of molecular gas, we have carried out several simulations in which we increased both G_0 and ζ_{H} by factors of 10 and 100 compared to our default values. The details of these runs are listed at the end of Table 1. In five of these runs, star formation begins after roughly 2–3 Myr, just as in the runs in which we keep ζ_{H} fixed. In run Z01-G100-CR100, however, the combination of the elevated ISRF and stronger cosmic ray flux provide so much heating that star formation is completely suppressed. The gas in the cloud heats up rapidly, with the mass-weighted mean temperature reaching $T \sim 1000$ K after only 1 Myr, and $T \sim 2400$ K after 2 Myr. This strong heating causes the cloud to expand, reducing its density and allowing the temperature to climb further, a process that eventually results in the destruction of the cloud. As a result of this, the C and CO abundances remain extremely small throughout the simulation. For this reason, we do not include this run in our further analysis.

For the remainder of the runs with elevated cosmic ray ionization rates, we compute X_{CI} and X_{CO} at t_{SF} and $t_1 \equiv t_{\text{SF}} - 1$ Myr. The results are shown in Table 4, along with the values from the corresponding runs with fixed ζ_{H} .

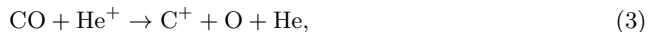
We see from Table 4 that an increase in ζ_{H} leads to an increase in X_{CO} and a decrease in X_{CI} . This behaviour is easy to understand chemically. As we increase the cosmic ray ionization rate, we increase the amount of He^+ present

Table 4. Comparison of X_{CI} and X_{CO} in runs with different cosmic ray ionization rates

ID	$X_{\text{CI}}(t_1)$	$X_{\text{CO}}(t_1)$	$X_{\text{CI}}(t_{\text{SF}})$	$X_{\text{CO}}(t_{\text{SF}})$
Z1-G10-CR10	2.46	2.04	4.61	2.01
Z1-G10	2.95	1.47	5.85	1.58
Z1-G100-CR100	2.87	11.7	3.18	3.02
Z1-G100	4.94	2.86	6.85	1.99
Z03-G10-CR10	36.3	48.1	20.9	7.35
Z03-G10	54.5	35.2	33.7	6.1
Z03-G100-CR100	85.3	2110	22.0	20.8
Z03-G100	326	810	64.5	15.7
Z01-G10-CR10	213	30500	85.6	25.1
Z01-G10	463	34300	132	15.0

X_{CI} and X_{CO} are given in units of the Galactic CO-to-H₂ conversion factor $X_{\text{CO,MW}}$ (see Eq. 1). Values are shown for t_{SF} and $t_1 \equiv t_{\text{SF}} - 1$ Myr.

in the gas. This in turn increases the rate at which CO is destroyed by the dissociative charge transfer reaction



which is the dominant destruction mechanism for CO in well-shielded gas. Increasing the cosmic ray ionization rate therefore reduces the amount of CO present in the cloud, which in turn reduces the mean CO brightness and increases X_{CO} . In well-shielded regions, the C⁺ produced by this reaction does not persist in the gas for long. Instead, it is converted to neutral atomic carbon by radiative recombination. The timescale for this process is much shorter than the timescale on which these carbon atoms are incorporated into new CO molecules, and so the end result is an increase in the C abundance, and hence an increase in W_{CI} and decrease in X_{CI} . Note also that although our chemical model does not include the reactions



and



we do not expect these reactions to significantly affect the atomic carbon abundance, despite the increased H⁺ and He⁺ abundances produced by the higher cosmic ray ionization rate. The reason for is that, in contrast to reaction 3, which proceeds at close to the Langevin rate (Anicich & Huntress 1986), reactions 4 and 5 occur only very slowly, since both have rate coefficients that are roughly a million times smaller than that of reaction 3 (Kimura et al. 1993; Stancil et al. 1998).

Looking in more detail at the values for X_{CI} and X_{CO} listed in Table 4, we see that at $t = t_{\text{SF}}$, even relatively large changes in the cosmic ray ionization rate lead to only comparatively small changes in the conversion factors. X_{CO} increases by less than a factor of two, even if we increase ζ_{H} by a factor of 100. X_{CI} is somewhat more sensitive to the value of ζ_{H} , but even in this case varies by no more than a factor of three for a factor of 100 change in the ionization rate. At earlier times in the evolution of the cloud, X_{CO} becomes more sensitive to ζ_{H} and X_{CI} becomes slightly less

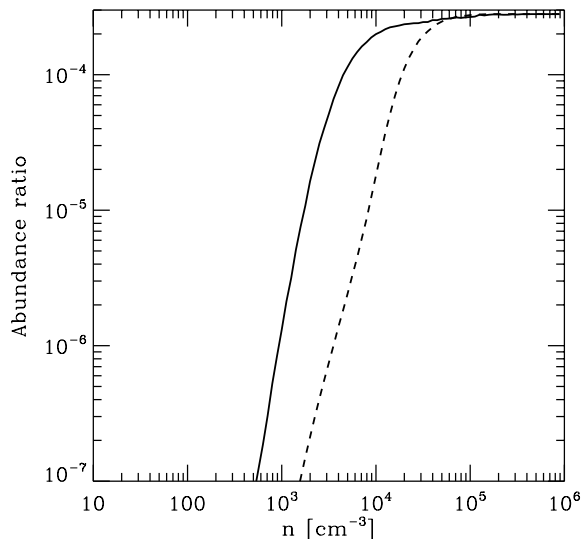


Figure 9. Ratio of the mean fractional abundances of CO and H₂, plotted as a function of the density, for runs Z1-G100 (solid line) and Z1-G100-CR100 (dashed line) at $t = t_{\text{SF}}$. Note that in fully molecular gas, our choice for the total carbon abundance implies that $x_{\text{CO}}/x_{\text{H}_2} = 2.8 \times 10^{-4}$.

sensitive, but again the largest differences we see are around a factor of a few. Therefore, the qualitative details of the results presented in the previous sections are robust against changes in the cosmic ray ionization rate, even though the quantitative details are not.

Finally, it is interesting to compare our results with the recent prediction by Bisbas, Papadopoulos, & Viti (2015) that cosmic ray ionization rates of around 10^{-16} – 10^{-15} s⁻¹ are sufficient to render molecular gas largely untraceable by CO at typical molecular cloud densities. As is clear from the results in Table 4, values of ζ_{H} in this range do increase X_{CO} slightly in evolved clouds, but the clouds are still bright in CO, which remains a good tracer of molecular gas at metallicities close to solar. Our results therefore do not confirm the Bisbas, Papadopoulos, & Viti (2015) prediction. The discrepancy between our study and theirs seems to arise from the difference in how we treat the density structure of the model clouds. Bisbas, Papadopoulos, & Viti largely focus on the effect of cosmic rays in uniform density clouds, and find that in this case, at typical GMCs densities of 100–1000 cm⁻³, CO is strongly suppressed when $\zeta_{\text{H}} \geq 10^{-16}$ s⁻¹ even in the absence of photodissociation. In our turbulent clouds, we also find low CO abundances in gas with this range of densities when ζ_{H} is large, as illustrated in Figure 9. In this respect, our model produces results in good agreement with the Bisbas, Papadopoulos, & Viti results. However, thanks to the influence of the turbulent velocity field, the density distribution inside our model clouds is highly inhomogeneous, with a significant mass fraction located in regions with a mean density substantially higher than the volume-weighted mean density of the cloud. For example, in run Z1-G100-CR100 at $t = t_{\text{SF}}$, almost 10% of the mass of the cloud is located in clumps with $n > 10^4$ cm⁻³, where both our model and the Bisbas, Papadopoulos, & Viti (2015) model agree that the carbon will be almost entirely locked up in CO. These dense clumps therefore remain CO-bright.

Moreover, since these clumps are distributed throughout much of the cloud, the mean CO brightness of the cloud as a whole remains high, with the consequence that X_{CO} remains close to its standard Galactic value. We can be confident that this is not simply due to some peculiarity of the model cloud studied here because our results for solar metallicity clouds are in reasonable agreement with those presented in the study of Clark & Glover (2015), which examined a wider range of cloud masses and densities and used a different random realization of the turbulent velocity field. Instead, this seems to be a general consequence of the presence of supersonic turbulence within the clouds. We note that the fact that the cloud inhomogeneity created by turbulence would allow more CO to survive was mentioned as a possible caveat by Bisbas, Papadopoulos, & Viti (2015), albeit in the context of clouds with higher than normal levels of turbulence. Our results show that this effect is important even in clouds with a ‘normal’ level of turbulence (i.e. ones which sit on the standard size-linewidth relation, as derived by e.g. Larson 1981 or Solomon et al. 1987).

3.6 Missing physics

Our models neglect several physical processes that will be active in real molecular clouds. The most important of these are the freeze-out of CO onto cold dust grains, the influence of the magnetic field on the dynamical evolution of the gas, and the effects of star formation and the associated feedback on the chemical, thermal and dynamical state of the cloud. In this section, we briefly discuss how these missing processes may affect our results.

3.6.1 Freeze-out

In dense gas, the mean time between collisions between a given gas-phase particle (e.g. an H_2 or CO molecule) and a dust grain can become shorter than the dynamical time of the gas. In this regime, the freeze-out of gas phase chemicals onto the surface of dust grains can become important, provided that the average residence time of these species on the grain surface is also long. The residence time depends sensitively on the binding energy of the species to the surface, and so H_2 , which binds only very weakly, does not freeze-out, while CO, which binds much more strongly, can become significantly depleted from the gas phase (see e.g. Bergin et al. 2002, for a good observational example).

The simplified chemical model that we use in our simulations does not account for the freeze-out of CO, and so the question arises as to whether this leads us to over-estimate the mean CO integrated intensity, and hence under-estimate X_{CO} . To investigate this, we have attempted to account approximately for the effects of CO freeze-out in an additional post-processing step. We make two important simplifying assumptions. First, we assume that locally, the ratio of gas-phase CO to CO ice has reached equilibrium. This is a reasonable assumption in dense gas, but means that we will overestimate the degree to which CO is depleted in diffuse gas, particularly at sub-solar metallicities. Second, we assume that the only processes that affect the ratio of gas-phase CO to CO ice are the accretion of CO molecules by dust grains, thermal desorption of the CO molecules and

cosmic-ray induced desorption due to local spot-heating of the grains. Our neglect of photodesorption, which is more difficult to model, again means that we will tend to overestimate the extent to which CO is depleted.

Having made these assumptions, we can relate the fractional abundance of gas-phase CO, $x_{\text{CO,gas}}$ to the fractional abundance of CO ice, $x_{\text{CO,ice}}$ using the following equation:

$$R_{\text{acc}}x_{\text{CO,gas}} = (R_{\text{therm}} + R_{\text{cr}})x_{\text{CO,ice}}. \quad (6)$$

Here, R_{acc} is the rate per CO molecule at which CO is accreted by dust grains, R_{therm} is the rate per CO molecule at which CO evaporates from the grain surfaces and R_{cr} is the rate per CO molecule at which CO is desorbed by cosmic rays. Following Hollenbach et al. (2009), we have

$$R_{\text{acc}} = 10^{-17}T^{1/2}\mathcal{D}n \text{ s}^{-1} \text{ molecule}^{-1}, \quad (7)$$

where n is the number density of hydrogen nuclei,

$$R_{\text{therm}} = 1.04 \times 10^{12} \exp\left(\frac{-960}{T_{\text{d}}}\right) \text{ s}^{-1} \text{ molecule}^{-1}, \quad (8)$$

where T_{d} is the dust temperature, and

$$R_{\text{cr}} = 6.0 \times 10^{-13}\zeta_{\text{H},17} \text{ s}^{-1} \text{ molecule}^{-1}, \quad (9)$$

where $\zeta_{\text{H},17} = \zeta_{\text{H}}/10^{-17} \text{ s}^{-1}$. The expression here for the thermal desorption rate assumes a CO adsorption energy of $E_{\text{D}}/k = 960 \text{ K}$, following Aikawa et al. (1996). The cosmic ray desorption rate is based on the calculations of Herbst & Cuppen (2006).

Armed with the depletion and desorption rates, we can write the ratio of gas-phase CO to CO ice as

$$\frac{x_{\text{CO,gas}}}{x_{\text{CO,ice}}} = \frac{R_{\text{therm}} + R_{\text{cr}}}{R_{\text{acc}}}. \quad (10)$$

For $T_{\text{d}} \ll 17 \text{ K}$, cosmic-ray desorption dominates over thermal desorption and this reduces to

$$\frac{x_{\text{CO,gas}}}{x_{\text{CO,ice}}} = \frac{R_{\text{cr}}}{R_{\text{acc}}} \simeq 6 \times 10^4 T^{-1/2} \frac{\zeta_{\text{H},17}}{\mathcal{D}n}. \quad (11)$$

In dense gas with $T = 15 \text{ K}$, $\mathcal{D} = 1$ and $\zeta_{\text{H},17} = 1$, we therefore expect that roughly half of the CO will be depleted once the gas density reaches $n \sim 15000 \text{ cm}^{-3}$. Observationally, the density at which $x_{\text{CO,gas}} \sim x_{\text{CO,ice}}$ is found to be a factor of a few larger than this (Lippok et al. 2013), demonstrating that, as expected, our simplified model overestimates the effectiveness of CO freeze-out.

To investigate the effect that freeze-out has on our predicted CO integrated intensities, we use the simplified model outlined above as part of an additional post-processing step. Before interpolating the CO densities from our SPH particles to the Cartesian grid that we use for our radiative transfer calculations, we first rescale them by a factor

$$F_{\text{gas}} = \frac{x_{\text{CO,gas}}}{x_{\text{CO,gas}} + x_{\text{CO,ice}}} = \frac{R_{\text{therm}} + R_{\text{cr}}}{R_{\text{therm}} + R_{\text{cr}} + R_{\text{acc}}} \quad (12)$$

to account for the effects of freeze-out, using the expressions for R_{acc} , R_{therm} and R_{cr} given in Equations 7–9 above. We then proceed as before, computing the CO emission from the cloud using RADMC-3D, and then using the mean values of the CO integrated intensity and H_2 column density to compute X_{CO} .

We have carried out this analysis for three of our cloud models, Z1-G1, Z02-G1 and Z003-G1, chosen to span the full range of metallicities examined in this study. We list the

Table 5. Comparison of X_{CO} computed with and without our approximate freeze-out model

ID	X_{CO}	
	Without freeze-out	With freeze-out
Z1-G1	1.33	1.36
Z02-G1	3.13	3.32
Z003-G1	21.9	28.5

X_{CO} is given in units of the Galactic CO-to-H₂ conversion factor $X_{\text{CO,MW}}$ (see Eq. 1) and is computed for $t = t_{\text{SF}}$.

resulting values of X_{CO} in Table 5, along with the values that we obtain in the absence of freeze-out. We see that at solar metallicity, freeze-out has a negligible effect on the predicted value of X_{CO} . This is easy to understand, as by the time we reach the densities at which CO freeze-out becomes significant, the gas is highly optically thick in the ¹²CO 1 → 0 line. Because the line is optically thick, removing even a large fraction of the CO has little effect on the total emission (provided that τ remains greater than one), and hence little effect on X_{CO} .

As we reduce the metallicity, we find that freeze-out starts to have a greater effect on X_{CO} . Again, this is easy to understand: at lower Z, we have much less CO and hence the optical depth of the line is much smaller, making it more sensitive to the actual CO abundance. On the other hand, reducing the dust-to-gas ratio, which is assumed in these models to scale with Z, reduces the freeze-out rate, since there is less dust for the CO molecules to freeze out onto. Consequently, in the lower metallicity models, the density at which $x_{\text{CO,gas}} \sim x_{\text{CO,ice}}$ is much higher than in run Z1-G1. As a result, freeze-out remains relatively unimportant in these models despite the lower optical depths, increasing X_{CO} by at most 30%.

Finally, what about the other simulations studied in this paper? In the other runs with $G_0 = 1$, we would expect to recover results intermediate between the Z1-G1 and Z003-G1 results, with the precise behaviour depending on the metallicity. In the runs with reduced dust-to-gas ratio, the effects of freeze-out will be smaller, since $R_{\text{acc}} \propto \mathcal{D}$. In the runs with $G_0 = 10$ or 100, we would again expect the effects of freeze-out to be smaller, since the dust will be warmer, making R_{therm} larger. Finally, in the runs with elevated cosmic ray ionization rates, R_{cr} will be larger, and so once again we will have less freeze-out. Therefore, it seems safe to conclude that the freeze-out of CO onto dust will not strongly affect the results we recover for the behaviour of X_{CO} in any of our cloud models.

3.6.2 Magnetic fields

Real molecular clouds are known to be magnetized (see e.g. Crutcher 2012), but we carry out our simulations using a purely hydrodynamical approach, in view of the technical difficulties involved in modeling magnetized gas with smoothed particle hydrodynamics (see the lengthy discussion in Price 2012). The question therefore arises as to how much this is likely to affect our results.

We know from previous simulations of turbulent molecular clouds (e.g. Padoan & Nordlund 2011; Molina et al. 2012) that prior to the onset of runaway gravitational col-

lapse, the width of the volume density and column density PDFs are sensitive to the strength of the magnetic field. Increasing the field strength provides additional resistance against compression or rarefaction and leads to a narrower volume density PDF. Projection of this into two dimensions then leads in turn to a narrower column density PDF. The extent to which this will affect $X_{\text{C I}}$ and X_{CO} will then depend on the size of the characteristic column density (or visual extinction) at which we find the transition from C⁺ to C or from C to CO. If this column density is comparable to or smaller than the mean column density of the cloud, then a significant fraction of the gas will be [C I] or CO rich, regardless of whether we consider a magnetized or unmagnetized cloud. In this case, we would expect the values of $X_{\text{C I}}$ and X_{CO} to be insensitive to the magnetic field strength. Similarly, if the required column density is so large that it is reached only in regions that go into runaway gravitational collapse (as in e.g. our low metallicity runs), then the amount of C and CO that form in the cloud will be insensitive to the width of the turbulence-dominated density PDF, implying that $X_{\text{C I}}$ and X_{CO} will also not vary much. The only case in which the difference in the width of the PDF is likely to have a large effect is if the characteristic column density is such that it is 1–2 standard deviations above the mean in the unmagnetized cloud, but multiple standard deviations above the mean in the magnetized cloud, owing to the change in the size of the standard deviation. In this case, we would go from predicting that the cloud is [C I] and CO-rich in the unmagnetized case to predicting that it is [C I] and CO-poor in the magnetized case. However, such a situation will rarely be encountered in practice, as magnetic fields of the level observed in most GMCs do not make a large difference to the width of the column density PDF. We therefore expect that accounting for this effect may lead to minor changes in our results at intermediate metallicities, but that it will not greatly change our main conclusions regarding the utility of [C I] and CO as tracers of molecular gas.

The other potentially important effect of the magnetic field will be to suppress the gravitational collapse of dense regions, if they are magnetically sub-critical. This can have a large effect on X_{CO} in low metallicity clouds: if gravitational collapse is suppressed, the gas will never become CO-bright, and so X_{CO} will remain large. Clouds that are so magnetically dominated that they remain starless for long periods will therefore also remain invisible in CO for long periods. In this circumstance, [C I] will clearly be a much better tracer of the clouds. However, it should also be noted that the importance of this effect is unclear. Measurements of the magnetic field strength in dense prestellar cores in local molecular clouds suggest that these cores are generally magnetically supercritical, and hence that gravitational collapse is not strongly suppressed (Troland & Crutcher 2008; Crutcher 2012). Whether the same holds true for dense clouds in much lower metallicity environments is unknown.

3.6.3 Star formation and feedback

Our simulations do not account for the effects of stellar feedback. Because of this, we cannot explore how $X_{\text{C I}}$ and X_{CO} evolve over the entire lifetime of one of our simulated clouds, as without feedback, there is nothing to stop the whole of

the gas eventually being converted to stars. We have therefore focussed primarily on their evolution prior to the onset of star formation (i.e. at $t < t_{\text{SF}}$), when stellar feedback is, by definition, completely absent.

However, in Section 3.2 we did investigate how X_{CO} and X_{CI} evolved in the interval between $t = t_{\text{SF}}$ and $t = t_{\text{SF}} + 0.5$ Myr in a few of our simulations, and it is therefore important to note that our results for this regime may be affected by our neglect of feedback. The importance of feedback during this period will depend on the star formation rate of the clouds and how much of the dense, CO-bright gas is actively forming stars. For example, in run Z1-G1, the star formation efficiency of the cloud at $t = t_{\text{SF}} + 0.5$ Myr is only around 0.3%, and much of the CO is located in gas which is too diffuse to be actively star-forming. In this cloud, we would not expect the evolution of X_{CO} and X_{CI} at $t > t_{\text{SF}}$ to have yet been strongly affected by stellar feedback. On the other hand, in run Z003-G100, the star formation efficiency of the cloud at $t = t_{\text{SF}} + 0.5$ Myr is around 7.8%, more than an order of magnitude larger than in the solar metallicity case. This difference in star formation efficiency is a consequence of the different thermal structure of the two clouds. The gas in the low metallicity, strongly irradiated cloud is significantly warmer than the gas in the solar metallicity cloud. This means that it takes longer to form a dense core which is sufficiently massive to be self-gravitating (see Table 2), but also that once such a core has formed, it is able to form a lot of stars relatively rapidly. Because of the high instantaneous star formation rate in this cloud, and the fact that all of the CO is located in a single dense core, it is plausible that if we were to include the effects of stellar feedback, much of the CO would be destroyed. In this case, the period during which the cloud is CO-bright would be even more short-lived than we find in our simulations. However, confirmation of this requires simulations that do account for the effects of stellar feedback, which are out of the scope of our present study.

4 CONCLUSIONS

The most important point to take away from this study is that the usefulness of [C I] emission as a tracer of H_2 mass in low metallicity clouds depends strongly on the evolutionary state of the clouds. At early times, prior to the onset of gravitational collapse in the cloud, [C I] is a far better tracer of H_2 than CO. The [C I]-to- H_2 conversion factor, X_{CI} , is not constant – it varies with the metallicity roughly as $X_{\text{CI}} \propto Z^{-1.5} - Z^{-2}$ for metallicities in the range $0.1 < Z/Z_{\odot} < 1.0$ – but it is far less sensitive to changes in the metallicity than CO, which is an extremely ineffective tracer of molecular mass in starless clouds at low metallicity.

Shortly before the onset of star formation, however, CO becomes a much better tracer of the molecular mass. At $t = t_{\text{SF}}$, both X_{CO} and X_{CI} scale approximately with metallicity as $X \propto Z^{-1}$, but X_{CO} is consistently smaller than X_{CI} , by a factor ranging from a few to an order of magnitude. Since it is much easier to observe the $^{12}\text{CO } J = 1 \rightarrow 0$ line in terrestrial conditions than the [C I] 609 μm line, the conclusion we draw from this is that at redshifts close to zero, CO should be preferred to [C I] as a tracer of the H_2 mass

of star-forming clouds in low metallicity systems.³ At higher redshifts, however, the [C I] 609 μm line becomes much easier to observe from the ground, and in this case [C I] can become competitive with CO as a tracer of molecular gas in metal-poor star-forming systems (Papadopoulos, Thi & Viti 2004).

The difference in the behaviour of starless and star-forming clouds can be understood as a consequence of the physical conditions required to form CO in low metallicity clouds. Substantial amounts of CO form only in gas with $A_V \sim 1$ or above. In low metallicity clouds, this gas is found only in dense, gravitationally collapsing cores. At early times in the evolution of the cloud, its structure is dominated by turbulence rather than gravity, and these dense cores are not present. Consequently, the mean CO brightness of the cloud at this time is extremely small. At later times, however, dense cores form due to gravitational instability, leading to a dramatic increase in the CO brightness of the cloud. On the other hand, the [C I] abundance is far less sensitive to the visual extinction, and so the mean [C I] brightness of the cloud varies much less as the cloud evolves.

We have also examined how our results change if we relax our assumption that the dust-to-gas ratio \mathcal{D} scales linearly with the gas-phase metallicity, and instead allow it to drop more rapidly with decreasing Z , as suggested by the available observational data. We find that in practice, this strengthens our results regarding the relative usefulness of CO and [C I] as molecular gas tracers. Significantly decreasing \mathcal{D} leads to a substantial decrease in the CO content of the clouds at early times, and hence a substantial increase in X_{CO} . On the other hand, it has little influence on the value of X_{CO} that we recover once star formation begins. At the same time, reducing \mathcal{D} also leads to a decrease in the amount of H_2 formed in the cloud, which acts to decrease X_{CO} , although this effect only seems to be important if the dust-to-gas ratio is very low.

Finally, we have examined the consequences of allowing the cosmic ray ionization rate to increase at the same time as the strength of the ISRF, as we would expect to occur if both directly track the star formation rate (see e.g. Clark & Glover 2015). We find that qualitatively, we recover similar results, but some of the quantitative details change. Notably, increasing the cosmic ray ionization rate by a factor of 10 or 100 has only a minor effect on the values of X_{CO} we recover for our star-forming clouds (contrary to the prediction of Bisbas, Papadopoulos, & Viti 2015), but can lead to a factor of two to three decrease in X_{CI} , improving our prospects for using [C I] emission to trace H_2 in these systems.

ACKNOWLEDGEMENTS

The authors thank the anonymous referee for a constructive report that helped them to improve the paper. They also acknowledge useful conversations with D. Cormier, S. Madden, and S. Malhotra on the topic of [C I] in metal-poor galaxies. SCOG acknowledges financial support from the Deutsche

³ Arguably, the [C II] 158 μm fine structure line is an even better tracer of H_2 in these systems (see e.g. Cormier et al. 2015), but this topic lies outside of the scope of this paper.

Forschungsgemeinschaft via SFB 881, “The Milky Way System” (sub-projects B1, B2 and B8) and SPP 1573, “Physics of the Interstellar Medium” (grant number GL 668/2-1).

REFERENCES

- Abreu-Vicente, J., Kainulainen, J., Stutz, A., Henning, Th., & Beuther, H. 2015, *A&A*, 581, A74
- Aikawa, Y., Miyama, S. M., Nakano, T., & Umebayashi, T. 1996, *ApJ*, 467, 684
- Anicich, V. G., & Huntress, W. T. 1986, *ApJS*, 62, 553
- Bate, M. R., Bonnell, I. A., & Price, N. M. 1995, *MNRAS*, 277, 362
- Benz, W., 1990, in ‘Proceedings of the NATO Advanced Research Workshop on The Numerical Modelling of Non-linear Stellar Pulsations Problems and Prospects’, ed. J. R. Buchler, (Dordrecht: Kluwer), 269
- Bergin, E. A., Alves, J., Huard, T., & Lada, C. J. 2002, *ApJ*, 570, L101
- Beuther, H., Ragan, S. E., Ossenkopf, V., Glover, S., Henning, Th., Linz, H., Nielbock, M., Krause, O., Stutzki, J., Schilke, P., & Güsten, R. 2014, *A&A*, 571, 53
- Bisbas, T. G., Bell, T. A., Viti, S., Yates, J., & Barlow, M. J. 2012, *MNRAS*, 427, 2100
- Bisbas, T. G., Papadopoulos, P. P., & Viti, S. 2015, *ApJ*, 803, 37
- Bolatto, A., et al., 2011, *ApJ*, 741, 12
- Bolatto, A. D., Wolfire, M., Leroy, A. K. 2013, *ARA&A*, 51, 207
- Burkhart, B., & Lazarian, A. 2012, *ApJ*, 755, L19
- Clark, P. C., Glover, S. C. O., & Klessen, R. S. 2012, *MNRAS*, 420, 745
- Clark, P. C., & Glover, S. C. O., 2015, *MNRAS*, 452, 2057
- Crutcher, R. M. 2012 *ARA&A*, 50, 29
- Cormier, D., et al., 2015, *A&A*, 578, A53
- Draine, B. T. 1978, *ApJS*, 36, 595
- Elmegreen, B. G., Rubio, M., Hunter, D. A., Verdugo, C., Brinks, E., & Schrubba, A. 2013, *Nature*, 495, 487
- Federrath, C., Roman-Duval, J., Klessen, R. S., Schmidt, W., & Mac Low, M.-M. 2010, *A&A*, 512, A81
- Frerking, M. A., Keene, J., Blake, G. A., Phillips, T. G., 1989, *ApJ*, 344, 311
- Galametz, M., Madden, S. C., Galliano, F., Hony, S., Bendo, G. J., & Sauvage, M. 2011, *A&A*, 532, 56
- Genzel, R., Harris, A. I., Stutzki, J., & Jaffe, D. T. 1988, *ApJ*, 332, 1049
- Glover, S. C. O., & Clark, P. C. 2012a, *MNRAS*, 421, 9
- Glover, S. C. O., & Clark, P. C. 2012b, *MNRAS*, 426, 377
- Glover, S. C. O., & Clark, P. C. 2012c, *MNRAS*, 421, 116
- Glover, S. C. O., & Mac Low, M.-M. 2007a, *ApJS*, 169, 239
- Glover, S. C. O., & Mac Low, M.-M. 2007b, *ApJ*, 659, 1317
- Glover, S. C. O., & Mac Low, M.-M. 2011, *MNRAS*, 412, 337
- Glover, S. C. O., Micic, M., Molina, F., & Clark, P. C. 2015, *MNRAS*, 448, 1607
- Glover, S. C. O., Federrath, C., Mac Low, M.-M., & Klessen, R. S. 2010, *MNRAS*, 404, 2
- Gordon, K. D., et al. 2014, *ApJ*, 797, 85
- Gratier, P., et al., 2010, *A&A*, 512, 68
- Herbst, E., & Cuppen, H. M. 2006, *Proc. Natl. Acad. Sci.*, 103, 12257
- Herrera-Camus, R., et al., 2012, *ApJ*, 752, 112
- Hollenbach, D., Kaufman, M. J., Bergin, E. A., & Melnick, G. J. 2009, *ApJ*, 690, 1497
- Israel, F. P. 1997, *A&A*, 328, 471
- Jappsen, A.-K., Klessen, R. S., Larson, R. B., Li, Y., Mac Low, M.-M. 2005, *A&A*, 435, 611
- Kainulainen, J., Beuther, H., Henning, T., & Plume, R. 2009, *A&A*, 508, L35
- Kimura, M., Dalgarno, A., Chantranupong, L., Li, Y., Hirsch, G., & Bunker, R. J. 1993, *ApJ*, 417, 812
- Klessen, R. S., 2000, *ApJ*, 535, 869
- Kramer, C., Jakob, H., Mookerjee, B., Schneider, N., Brüll, M., & Stutzki, J. 2004, *A&A*, 424, 887
- Kramer, C., et al., 2008, *A&A*, 477, 547
- Langer, W., 1976, *ApJ*, 206, 699
- Larson, R. B., 1981, *MNRAS*, 194, 809
- Lee, M.-Y., Stanimirović, S., Wolfire, M. G., Shetty, R., Glover, S. C. O., Molina, F. Z., & Klessen, R. S. 2014, *ApJ*, 784, 80
- Leroy, A., Bolatto, A., Stanimirovic, S., Mizuno, N., Israel, F., & Bot, C. 2007, *ApJ*, 658, 1027
- Leroy, A., et al., 2011, *ApJ*, 737, 12
- Lippok, N., et al. 2013, *A&A*, 560, A41
- Little, L. T., Gibb, A. G., Heaton, B. D., Ellison, B. N., Claude, S. M. X., 1994, *MNRAS*, 271, 649
- Madden, S. C., Poglitsch, A., Geis, N., Stacey, G. J., & Townes, C. H., 1997, *ApJ*, 483, 200
- Mathis, J. S., Mezger, P. G., & Panagia, N. 1983, *A&A*, 128, 212
- Molina, F. Z., Glover, S. C. O., Federrath, C., & Klessen, R. S. 2012, *MNRAS*, 423, 2680
- Narayanan, D., Krumholz, M., Ostriker, E. C., & Hernquist, L. 2011, *MNRAS*, 418, 664
- Narayanan, D., Hopkins, P. F., 2013, *MNRAS*, 433, 1223
- Nelson, R. P., & Langer, W. D. 1999, *ApJ*, 524, 923
- Offner, S. S. R., Bisbas, T. G., Viti, S., & Bell, T. A. 2013, *ApJ*, 770, 49
- Offner, S. S. R., Bisbas, T. G., Bell, T. A., & Viti, S. 2014, *MNRAS*, 440, L81
- Padoan, P., & Nordlund, Å, 2011, *ApJ*, 730, 40
- Papadopoulos, P. P., 2010, *ApJ*, 720, 226
- Papadopoulos, P. P., Thi, W.-F., & Viti, S. 2004, *MNRAS*, 351, 147
- Papadopoulos, P. P., Thi, W.-F., Miniati, F., & Viti, S. 2011, *MNRAS*, 414, 1705
- Pineda, J. E., Caselli, P., & Goodman, A. A. 2008, *ApJ*, 679, 481
- Plume, R., Jaffe, D. T., & Keene, J. 1994, *ApJ*, 425, L49
- Price, D. J. 2012, *J. Comp. Phys.*, 231, 759
- Rémy-Ruyer, A., et al. 2014, *A&A*, 563, A31
- Roman-Duval, J., Jackson, J. M., Heyer, M., Rathborne, J., & Simon, R. 2010, *ApJ*, 723, 492
- Sandstrom, K. M., et al. 2013, *ApJ*, 777, 5
- Schilke, P., Keene, J., Le Bourlot, J., Pineau des Forets, G., Roueff, E., 1995, *A&A*, 294, L17
- Schneider, N., Simon, R., Kramer, C., Kraemer, K., Stutzki, J., & Mookerjee, B. 2003, *A&A*, 406, 915
- Schneider, N., Csengeri, T., Klessen, R. S., Tremblin, P., Ossenkopf, V., Peretto, N., Simon, R., Bontemps, S., & Federrath, C. 2015, *A&A*, 578, A29
- Sembach, K. R., Howk, J. C., Ryans, R. S. I., & Keenan, F. P. 2000, *ApJ*, 528, 310

- Shetty, R., Glover, S. C., Dullemond, C., & Klessen, R. S. 2011a, MNRAS, 412, 1686
- Shetty, R., Glover, S. C. O., Dullemond, C. P., Ostriker, E. C., Harris, A. I., & Klessen, R. S., 2011b, MNRAS, 415, 3253
- Shi, Y., Wang, J., Zhang, Z.-Y., Gao, Y., Armus, L., Helou, G., Gu, Q., & Stierwalt, S. 2015, ApJ, 804, L11
- Smith, M. W. L., et al., 2012, ApJ, 756, 40
- Solomon, P. M., Rivolo, A. R., Barrett, J., & Yahil, A. 1987, ApJ, 319, 730
- Springel, V. 2005, MNRAS, 364, 1105
- Stancil, P. C., Havener, C. C., Krstić, P. S., Schultz, D. R., Kimura, M., Gu, J.-P., Hirsch, G., Buenker, R. J., & Zygelman, B. 1998, ApJ, 502, 1006
- Stutzki, J., Stacey, G. J., Genzel, R., Harris, A. I., Jaffe, D. T., & Lugten, J. B. 1988, ApJ, 332, 379
- Troland, T. H., & Crutcher, R. M. 2008, ApJ, 680, 457
- Woodall, J., Agúndez, M., Markwick-Kemper, A. J., & Millar, T. J. 2007, A&A, 466, 1197